Energy Storage Materials 37 (2021) 47–54

Contents lists available at ScienceDirect

Energy Storage Materials

journal homepage: www.elsevier.com/locate/ensm

Short communication

Na_2ZrCl_6 enabling highly stable 3 V all-solid-state Na-ion batteries

Hiram Kwak[a,b,1], Jeyne Lyoo[c,1], Juhyoun Park[a,b], Yoonjae Han[a,b], Ryo Asakura[d], Arndt Remhof[d], Corsin Battaglia[d], Hansu Kim[b], Seung-Tae Hong[c,*], Yoon Seok Jung[a,*]

[a] Department of Chemical and Biomolecular Engineering, Yonsei University, Seoul 03722, South Korea
[b] Department of Energy Engineering, Hanyang University, Seoul 04763, South Korea
[c] Department of Energy Science and Engineering, DGIST (Daegu Gyeongbuk Institute of Science and Technology), Daegu 42988, South Korea
[d] Empa, Swiss Federal Laboratories for Materials Science and Technology, 8600 Dübendorf, Switzerland

ARTICLE INFO

Keywords:
All-solid-state batteries
Solid electrolytes
Halides
Ionic conductivities
Na-ion batteries

ABSTRACT

Halide solid electrolytes (SEs) are emerging as an alternative to sulfide and/or oxide SEs for applications in all-solid-state batteries owing to the advantage fulfilling high (electro)chemical stability and mechanical sinterability at the same time. Thus far, the developments in halide SEs have focused on Li^+ superionic conductors. Herein, the development of a new Na^+-conducting halide SE, mechanochemically prepared Na_2ZrCl_6 (1.8×10^{-5} S cm^{-1} at 30°C) with excellent oxidative electrochemical stability, is described. A trigonal crystal structure with the $P\bar{3}m1$ symmetry is successfully identified by the Rietveld refinement of X-ray diffraction. Additionally, the bond valence sum energy level calculations disclose one-dimensional preferable Na^+-diffusion channels in Na_2ZrCl_6. It is to be noted that despite the rather low Na^+ conductivity of Na_2ZrCl_6, $NaCrO_2$ electrodes that uses Na_2ZrCl_6 in $NaCrO_2$/Na-Sn all-solid-state Na-ion batteries demonstrate an exceptionally high initial Coulombic efficiency of 93.1% and a high reversible capacity of 111 mA h g^{-1} at 0.1C and 30 °C (98.4% and 123 mA h g^{-1} at 60 °C), highlighting the excellent electrochemical stability of Na_2ZrCl_6.

1. Introduction

All-solid-state batteries that use inorganic Na^+ superionic conductors hold a potential of better safety and lower cost, compared to conventional lithium-ion batteries based on organic liquid electrolytes [1-16]. Inorganic Na^+ solid electrolyte (SEs) materials include oxides (e.g., $Na_3Zr_2Si_2PO_{12}$, 0.4-1 mS cm^{-1}),[13-15] sulfides (e.g., Na_3PS_4, Na_3SbS_4, 0.1-10 mS cm^{-1}),[1,3,5,7,9] and closo-borates (e.g. $Na_4(B_{12}H_{12})(B_{10}H_{10})$, 1 mS cm^{-1}) [4]. Despite the acceptable (electro)chemical stabilities, oxide SEs suffer from poor contacts with electrode active materials when fabricating all-solid-state batteries [1,5]. In this regards, sulfide materials have drawn significant attention [1,3,5,7,9,16-18]. This is in the same vein of the preceding developments of Li^+-conducting sulfide counterparts (e.g., Li_6PS_5X, X = Cl, Br) showing the high ionic conductivities (10^{-3}–10^{-2} S cm^{-1}) and the deformable properties that are vital for achieving practical all-solid-state batteries [5,11,19-22].

Cubic Na_3PS_4 was the first sulfide-based Na^+ superionic conductor to be developed, exhibiting a conductivity of 0.2 mS cm^{-1} at room temperature;[1] thereafter, extensive efforts have focused on enhancing the Na^+ conductivity by examining the compositions based on Na_3PS_4 via substitution [17,18,23-25]. The isovalent substitution of P^{5+} with Sb^{5+} and As^{5+} [3,25] or S^{2-} with Se^{2-} [24] led to improvements in the ionic conductivity. Unlike the tetragonal phase (~10^{-6} S cm^{-1}) obtained by the conventional solid-state reaction, the mechanochemically derived cubic phase was initially attributed to the high ionic conductivity of Na_3PS_4 [1]. It was thereafter theoretically and experimentally determined that the formation of vacancies is crucial for the fast Na^+ transport in this class of sulfide superionic conductors [17,18,26,27]. Na^+ conductivities of ~1 mS cm^{-1} for Na_3PS_4-derived compositions were obtained by the aliovalent substitutions of Na^+ with Ca^{2+},[17] S^{2-} with Cl^-,[18] and P^{5+} with Sn^{4+} or Si^{4+} [8,23,26,28-30].

A limitation to be noted is that phosphorus-based sulfide SEs are prone to toxic H_2S gas evolution upon exposure to humid air [5,20]. It was observed that phosphorus-free Sb-based sulfide Na^+-conducting SE materials, such as Na_3SbS_4, $Na_{4-x}Sn_{1-x}Sb_xS_4$, and $Na_{3-x}Sb_{1-x}W_xS_4$ do not suffer from the evolution of H_2S gas [3,8,9]. Furthermore, our group demonstrated that water could be utilized for the liquid-phase synthesis of Na_3SbS_4 and $Na_{4-x}Sn_{1-x}Sb_xS_4$ [16]. However, the use of heavy elements may offset the advantage of phosphorus-free sulfide SE materials. Moreover, sulfide SE materials exhibit intrinsically narrow electrochemical windows [30-32]. In contact with layered oxide cathode materials that are used for either lithium- or sodium-ion batteries, the sulfide SE materials undergo severe side reactions, resulting in unsatisfactory elec-

* Corresponding author.
E-mail addresses: st.hong@dgist.ac.kr (S.-T. Hong), yoonsjung@yonsei.ac.kr (Y.S. Jung).

[1] These authors contributed equally.

https://doi.org/10.1016/j.ensm.2021.01.026
Received 19 October 2020; Received in revised form 16 January 2021; Accepted 26 January 2021
Available online 28 January 2021
2405-8297/

trochemical performances [5,30,32-34]. In particular, Na^+-conducting sulfide SEs did not exhibit sufficient stability with the 3 V-class oxide cathode materials, such as $NaCrO_2$ [3,35].

Recently emerging halide SEs show potential for applications in all-solid-state batteries, owing to their high (electro)chemical stability and deformability. These properties were not achieved in the previously investigated single SE materials of sulfides or oxides [36-38]. A study by Asano and coworkers on the mechanochemically prepared hexagonal close-packed (hcp)-structure trigonal Li_3YCl_6 and cubic close-packed (ccp)-structure monoclinic Li_3YBr_6 reported the conductivities of 0.51 and ~1 mS cm^{-1}, respectively. The results of their study were referenced by the identification of alternative Li^+ superionic halide conductors,[38-44] including Li_3ErCl_6 (0.31 mS cm^{-1}),[44] monoclinic Li_3InCl_6 (1.49 mS cm^{-1}),[39] monoclinic Li_xScCl_{3+x} (maximum 3 mS cm^{-1}),[41] disordered spinel $Li_2Sc_{2/3}Cl_4$ (1.5 mS cm^{-1}),[42] orthorhombic Zr^{4+}-substituted Li_3YCl_6 or Li_3ErCl_6 (max. ~1 mS cm^{-1}),[40] and trigonal Fe^{3+}-substituted Li_2ZrCl_6 [43]. Uncoated $LiCoO_2$ in all-solid-state cells using halide SEs, such as Li_3YCl_6, exhibited excellent initial Coulombic efficiency (94%) and stable cycling [38]. Notably, the high Li^+ conductivities of Li_3YCl_6 and Li_3ErCl_6 were obtained by mechanochemical milling [44]. Zeier and coworkers suggested that from the analysis of the pair distribution function, the disordering in metal sites (M2/M3) was the key to the significant enhancement of the Li^+ conductivity upon mechanochemical milling [44]. Despite the important advancements in Li^+-conducting halide SEs, the use of expensive central atoms, especially rare-earth metals, hinders their practical application. This aspect is highly critical in all-solid-state Na-ion batteries.

Herein, we report a new Na^+-conducting halide SE, Na_2ZrCl_6, prepared by a mechanochemical method. It exhibits a Na^+ conductivity of 1.8×10^{-5} S cm^{-1} at 30°C. A trigonal crystal structure of the $P\bar{3}m1$ symmetry with one-dimensional (1D) Na^+ diffusion channels was identified by the Rietveld refinement of X-ray diffraction (XRD) and bond valence energy landscape (BVEL) calculations. Despite the relatively low Na^+ conductivity of Na_2ZrCl_6, a 3 V-class $NaCrO_2$ electrode that uses Na_2ZrCl_6 in all-solid-state cells significantly outperforms the one which uses conventional sulfide SE, cubic Na_3PS_4. The Na^+ conductivity of the latter is one order of magnitude higher (1×10^{-4} S cm^{-1}).

2. Results and discussion

Two Na_2ZrCl_6 powders were prepared by ball-milling a stoichiometric mixture of NaCl and $ZrCl_4$ with and without subsequent heat treatment at 400 °C, and were denoted as HT-Na_2ZrCl_6 and BM-Na_2ZrCl_6, respectively. The Na^+ conductivities of the cold-pressed pellet samples were measured by the AC impedance method using Na^+-blocking Ti/SE/Ti symmetric cells. Fig. 1a shows the Arrhenius plots of the Na^+ conductivities for BM- and HT-Na_2ZrCl_6. The corresponding Nyquist plots are shown in Figure S1. BM-Na_2ZrCl_6 exhibited a Na^+ conductivity of 1.8×10^{-5} S cm^{-1} at 30 °C with an activation energy of 0.40 eV. The Na^+ conductivity is approximately one order of magnitude lower than that of cubic Na_3PS_4 (1.0×10^{-4} S cm^{-1}). For the heat-treated sample, a considerably lower Na^+ conductivity of 6.9×10^{-8} S cm^{-1} and a higher activation energy of 0.49 eV were obtained. The drastic change observed in the Na^+ conductivity upon heat treatment is similar to that observed for Li_3YCl_6 [38, 44]. The electron conductivity of BM-Na_2ZrCl_6, measured by chronoamperometry using the Ti/SE/Ti symmetric cell was 2.1×10^{-10} S cm^{-1}, which is more than five orders of magnitude lower than the Na^+ conductivity (Figure S2). Therefore, BM-Na_2ZrCl_6 can be regarded as a good solid electrolyte.

The powder XRD patterns of BM- and HT-Na_2ZrCl_6 are shown in Fig. 1b. BM-Na_2ZrCl_6 exhibited broad main reflections. These reflections are commonly observed in mechanochemically prepared samples, and indicate low crystallinity and/or structural disorder [38,39,44]. The main reflections for BM-Na_2ZrCl_6 at ~15, 30, and 39° match well those for Li_3YCl_6 or Li_3ErCl_6, which crystallize in a trigonal lattice with hcp anion sublattices (space group $P\bar{3}m1$, Figure S3) [38,44]. The slight shifts of the Bragg reflections to lower angles indicate larger lattice parameters of Na_2ZrCl_6, which can be attributed to the larger ionic size of Na^+ (102 pm) as compared to that of Li^+ (72 pm). In Li^+-conducting halide SEs, a ccp monoclinic lattice structure was observed in the compounds when central metal ions with smaller ionic radii, including Sc^{3+} (72 pm) [41,45] and In^{3+} (80 pm),[39] were employed. On the other hand, compounds comprising metal ions with larger ionic radii, such as Y^{3+} (90 pm), Tb^{3+} (92.3 pm), and Lu^{3+} (86.1 pm), form the hcp structure [38,45]. Despite the use of Zr^{4+} ions with small ionic radii (72 pm), the occurrence of the hcp trigonal structure for Na_2ZrCl_6, and the absence of it in the ccp monoclinic structure can be ascribed to the larger ionic size of Na^+ compared to that of Li^+. It was also observed that the position of the main reflections for BM-Na_2ZrCl_6 in the XRD pattern coincides with those for HT-Na_2ZrCl_6 (Fig. 1b), indicating that the two samples belong to the same parent structural framework [38, 44]. Thus, extensive structural analysis by powder XRD with Cu $K\alpha_1$ X-ray radiation was performed for HT-Na_2ZrCl_6 [38].

The powder X-ray Rietveld refinement profile for HT-Na_2ZrCl_6 is shown in Fig. 2a, and the corresponding results are summarized in Table 1. All the reflections can be indexed as the trigonal crystal structure with $P\bar{3}m1$ symmetry (a = 11.4861 (1) Å, c = 6.2768 (1) Å, V = 717.15 (1) $Å^3$, and Z = 3) that is isostructural with trigonal Li_3YCl_6

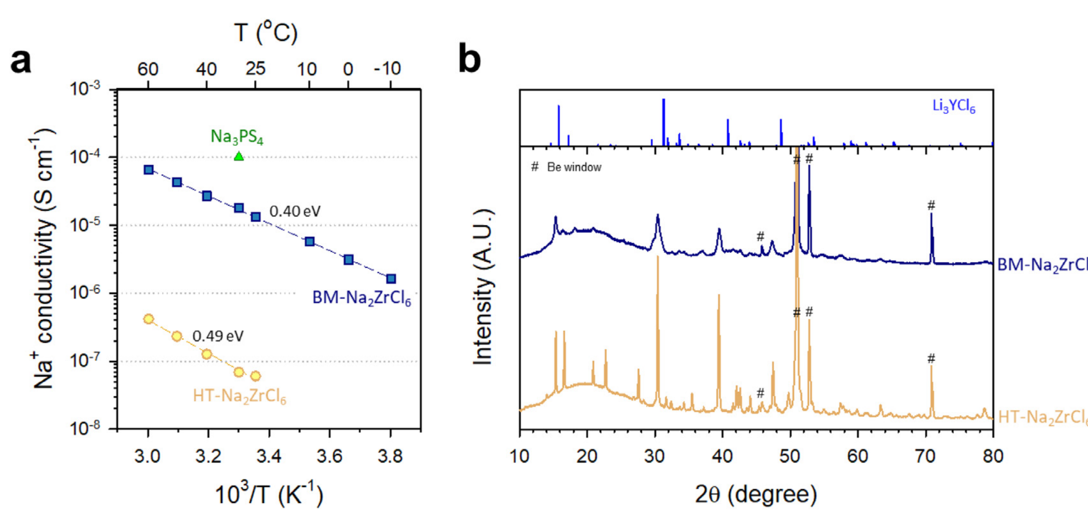

Fig. 1. Characterization of BM- and HT-Na_2ZrCl_6. a) Arrhenius plots of Na^+ conductivity and b) powder XRD patterns for BM- and HT-Na_2ZrCl_6. The Bragg reflections for Li_3YCl_6 (ref. 38) are shown at the top.

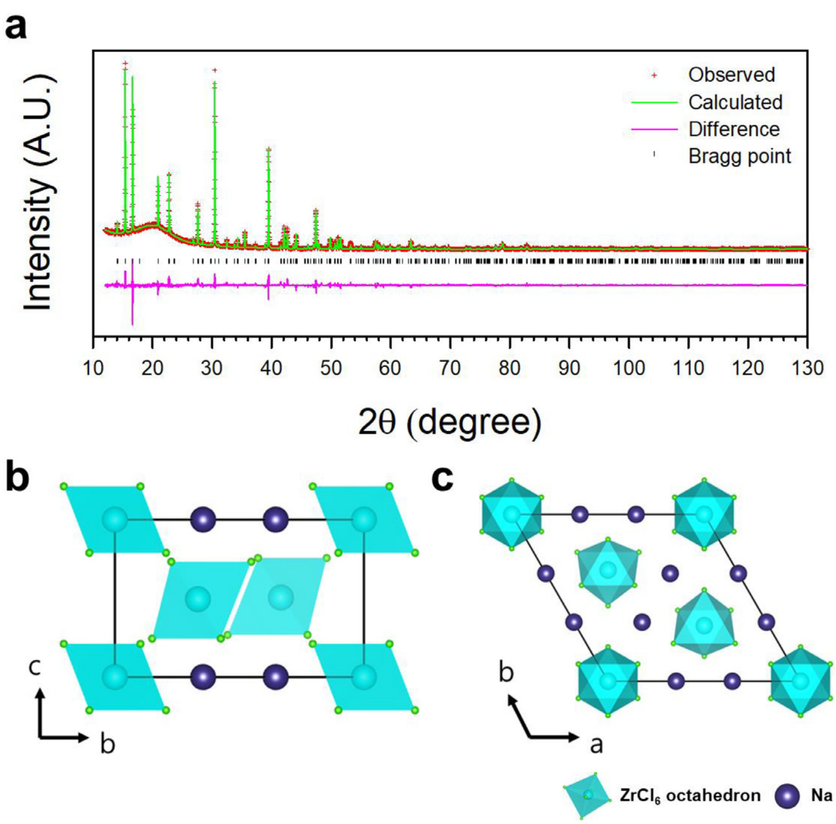

Fig. 2. Results of Cu Kα_1 XRD for HT-Na_2ZrCl_6. a) Observed and calculated powder X-ray Rietveld refinement profile for HT-Na_2ZrCl_6, recorded at 25°C. Bragg positions for Na_2ZrCl_6 are also shown. Crystal structure of Na_2ZrCl_6, showing b) (100) and c) (001) views where the unit cells are outlined.

Table 1
Crystallographic data and powder XRD Rietveld refinement results for Na_2ZrCl_6.

Crystal System	Trigonal					
Space Group	P $\bar{3}$ m 1 (no. 164)					
Lattice Parameter, Volume, Z	a = 11.4861 (1) Å, c = 6.2768 (1) Å, V = 717.15 (1) Å^3, Z = 3					
Atom	x	y	z	Wyckoff	Occupancy	U_{iso} × 100
Zr1	0	0	0	1 a	1.0	2.67 (1)
Zr2	$^1/_3$	$^2/_3$	0.4974 (8)	2 d	1.0	2.67 (1)
Cl1	0.2347 (1)	0.7654 (1)	0.2632 (7)	6 i	1.0	2.67 (1)
Cl2	0.1097 (1)	0.8903 (1)	0.8022 (1)	6 i	1.0	2.67 (1)
Cl3	0.5727 (4)	0.4274 (1)	0.2433 (7)	6 i	1.0	2.67 (1)
Na	0.3574 (5)	0	0	6 g	1.0	2.67 (1)

*R_p = 0.0795, R_{wp} = 0.1182, R_{exp} = 0.0816, R(F^2) = 0.1965, χ^2 = 2.102

and Li_3ErCl_6 [38, 44]. The atom positions in the unit cell were confirmed from the observed Fourier map (Figure S4). All the atoms of Na, Zr, and Cl were easily distinguishable because of the distinct differences in their electron densities. The crystal structure is visualized with two different orientations in Fig. 2b, c. The lattice framework of Na_2ZrCl_6 is similar to that of previously reported trigonal Li_3ErCl_6 (or Li_3YCl_6); however, the Na^+ ions are fully occupied in one crystallographic Wyckoff site (6g) for Na_2ZrCl_6, while Li^+ ions occupy two sites (fully occupied in 6g and half occupied in 6h) for Li_3ErCl_6. We noted that the 6h site is present in the midway between the two 6g sites parallel to the c-axis, and plays a role of interconnecting the 6g sites. Na_2ZrCl_6 consists of three $ZrCl_6$ octahedra and six Na atoms per unit cell. One $ZrCl_6$ octahedron is located in the ab-plane at z = 0, and the others are located at z ≈ 0.5. Na^+ ions also form a slightly distorted octahedron with halide ions. The $ZrCl_6$ octahedron at z = 0 is surrounded by six Na^+ ions that form a honeycomb lattice of $NaCl_6$ octahedra, whereas the $ZrCl_6$ octahedra at z ≈ 0.5 have no surrounding Na atoms. The average interatomic distance of d(Na–Cl) is 2.76 Å (Table S1), which is lower than the expected value (2.83 Å) from Shannon's ionic radii; [46] such a short interatomic distance may indicate strong binding between the Na^+ and Cl^- ions. Moreover, the Na site exhibits 100% occupancy without undergoing any disordering. To summarize, the strong binding between Na^+ and Cl^- and the lack of the interconnecting Na atom in the 6h site could be responsible for the low Na^+ conductivity of HT-Na_2ZrCl_6.

The Raman spectra of BM-Na_2ZrCl_6 and HT-Na_2ZrCl_6, compared with those of precursor $ZrCl_4$, are also shown in Figure S5. For $ZrCl_4$, the characteristic signatures of the zigzag polymer-like chain-structured $[(ZrCl_{4/2})Cl_2]_n$ of the bridged octahedra are shown [47]. In contrast, both BM- and HT-Na_2ZrCl_6 showed that the signatures of the bridging octahedra disappeared; strong peaks at ~320 cm^{-1}, which are attributed to A_{1g} stretching and generally observed for a series of elpasolite compounds, are indicative of $ZrCl_6{}^{2-}$ [48,49].

The bond valence sum has been widely used to estimate valences in inorganic solids for verifying the validity of the crystal structure [50]. The bond valence sums for each atom in Na_2ZrCl_6 were calculated: Na1 (1.10 valence unit; v.u), Zr1 (3.62 v.u), Zr2 (3.93 v.u), Cl1 (0.99 v.u), Cl2 (0.96 v.u), Cl3 (1.07 v.u), all of which match well with the expected ion charges. To better understand the Na^+ migration pathways in Na_2ZrCl_6, the BVEL calculation was also employed [3,8,51,52]. The BVEL map for Na_2ZrCl_6, using the structural parameters from Rietveld refinement (Fig. 3a, b, c), visualizes the possible Na^+ migration pathways. From this result, in addition to the Na1 site, a Na interstitial site ($Na_{int.}$) bridging

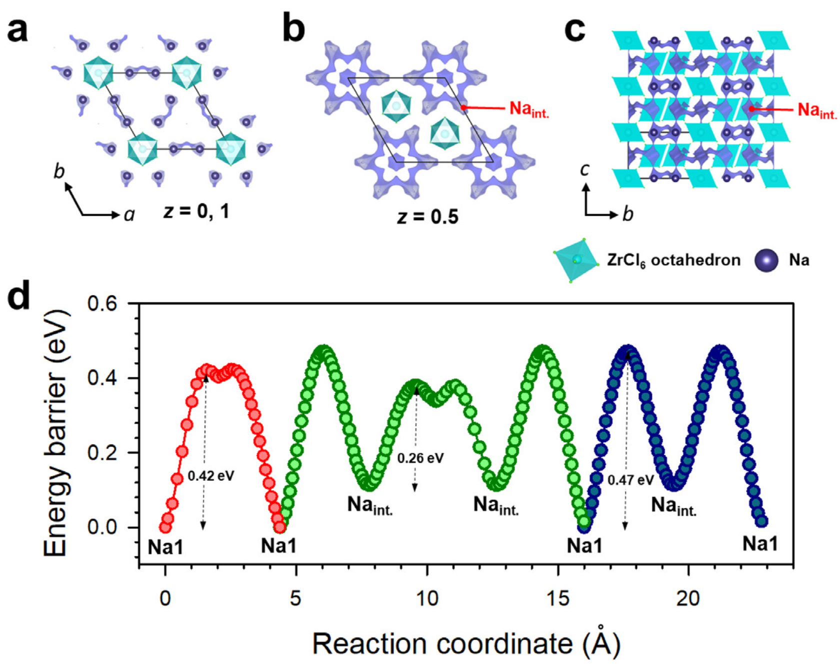

Fig. 3. BVEL calculation results for Na_2ZrCl_6. a-c) Na^+ diffusion paths for Na_2ZrCl_6 obtained by the BVEL calculations with an iso-surface value of 0.47 eV and d) energy landscape diagram for Na_2ZrCl_6, showing the migration barriers between Na^+ and interstitial sites determined from the BVEL calculations.

the 6g sites parallel to the c-axis can be identified near (0.325, 0, 0.5) in the distorted Cl^- surrounding octahedra, which corresponds to the 6h site. As shown in Fig. 3a, in the view of the ab-plane at z = 0, the Na^+ migration pathways are restricted to two neighboring Na1–Na1 sites. In the view of the ab-plane at z = 0.5 (Fig. 3b), the six $Na_{int.}$ sites create ribbon-shaped migration pathways with a low activation energy of 0.26 eV (Fig. 3d). However, Na^+ ions cannot diffuse over long distances because they cannot migrate to the neighboring ribbons. The interatomic distance between the two Na1 atoms along the c-axis is large (6.28 Å) for direct Na^+-hopping to occur. However, the $Na_{int.}$ site between the two Na1 atoms acts as a bridge, and the average interatomic distance for Na1–$Na_{int.}$, 3.17 Å, is a reasonable hopping distance. Thus, Na^+ migration would easily occur through Na1–$Na_{int.}$–Na1–$Na_{int.}$ along the c-axis. Considering that Na^+ cannot migrate over long distances in the ab-plane and Na1–$Na_{int.}$–Na1–$Na_{int.}$ pathways are formed in the [001] direction, Na_2ZrCl_6 likely prefers the 1D Na^+ migration pathways. The activation energy for the Na1–$Na_{int.}$–Na1 pathway parallel to the c-axis was calculated to be 0.47 eV (Fig. 3d). This value agrees well with that obtained using the AC impedance method (HT-Na_2ZrCl_6, 0.49 eV, Fig. 1a).

In previous reports on trigonal Li^+-conducting halide SEs, such as Li_3YCl_6 and Li_3ErCl_6, it was reported that the ball-milled samples exhibited higher ionic conductivities than the heat-treated samples, which was interpreted as the consequence of M2/M3 site disordering [38,44]. Considering the too large interatomic distance between the two Na1 atoms along the c-axis in HT-Na_2ZrCl_6, we anticipate the 1D Na^+ migration could be facilitated, if Na_{int} sites could be partially occupied, via the concerted or correlated interstitial (knock-on) mechanism [53-56]. We speculate the mechanochemical-milling would drive disordering of both M and Na^+ sites. And this might lead to a partial occupation of Na_{int} as well as a reconfiguration of Na^+ channels,[44] which could result in regulated energy landscape for more facilitated Na^+ migration and thus drastically enhanced Na^+ conductivity, as compared to HT-Na_2ZrCl_6 (from 6.9×10^{-8} to 1.8×10^{-5} S cm^{-1}). Alternatively, aliovalent substitution to increase Na contents may also be effective on enhancing Na^+ conductivity of Na_2ZrCl_6. Based on theoretical calculations, Mo and co-workers showed that ionic conductivities are highly affected by the concentration and distribution of cations in halide SEs [53]. Recently, our group reported that mechanochemically prepared Li_2ZrCl_6 showed the trigonal structure like Na_2ZrCl_6 in this work and its Li^+ conductivity could be more than doubled by the aliovalent substitution with trivalent metals, such as Fe^{3+}, V^{3+}, and Cr^{3+} (from 4.0×10^{-4} to max. $\sim 1 \times 10^{-3}$ S cm^{-1}), demonstrating the importance of charge carrier of mobile ions [43].

It is also noted that the size effect of the alkali ions may be more substantial in halide SEs, as compared with sulfide SEs, as the anionic framework for halide SEs is based on close-packed structure while that for sulfide SEs is based on base centered cubic in many cases [53,57]. Comparing Na_2ZrCl_6 with the Li counterpart, Li_2ZrCl_6, the lattice volume is increased by only 12% (HT-Na_2ZrCl_6: 2.43 g cm^{-3}, BM-Li_2ZrCl_6: 2.48 g cm^{-3}) [43]. It is thus considered that over an order of magnitude lower ionic conductivity of BM-Na_2ZrCl_6 (1.8×10^{-5} S cm^{-1}) than the Li counterparts including BM-Li_2ZrCl_6 (4.0×10^{-4} S cm^{-1}) might be largely attributed to the larger ionic size of Na^+ (102 pm) than that of Li^+ (72 pm) [58].

Electrochemical stability of BM-Na_2ZrCl_6 was assessed via cyclic voltammetry measurements using Ti/Na_2ZrCl_6/Na_3PS_4/Na-Sn cells (Figure S6). BM-Na_2ZrCl_6 showed poor cathodic stability with the onset voltage of ∼1.3 V (vs. Na/Na^+) for reduction but excellent oxidation stability up to 5 V (Na/Na^+), which is in line with other halide SEs [36-40].

Finally, $NaCrO_2$ electrodes fabricated using BM-Na_2ZrCl_6 (1.8×10^{-5} S cm^{-1}) or Na_3PS_4 (1.0×10^{-4} S cm^{-1}) in $NaCrO_2$/Na-Sn all-solid-state cells were cycled between 1.4 and 3.5 V at 30 °C. No carbon additives were used in the electrodes. To stabilize the SE/Na-Sn interfaces, a hybrid SE layer of $Na_3PS_4/Na_4(B_{12}H_{12})(B_{10}H_{10})$ was used such that the $Na_4(B_{12}H_{12})(B_{10}H_{10})$ (1.8×10^{-3} S cm^{-1}) side maintained contact with the Na-Sn anode (nominal composition of Na_3Sn, ∼0.1 V (vs. Na/Na^+)) [59,60]. Fig. 4a shows the first-cycle charge–discharge voltage profiles at 0.1C (1C = 120 mA g^{-1}). While no noticeable differences were observed in the initial charge, discharge capacity was much lower when using Na_3PS_4, as compared to when using BM-Na_2ZrCl_6 (90 vs. 111 mA h g^{-1}), reflecting highly irreversible reaction of Na_3PS_4. It is to be noted that the initial Coulombic efficiency (ICE) for using BM-Na_2ZrCl_6 was extremely high: 93.1%, which is comparable to that of conventional liquid electrolytes [61]. $NaCrO_2$/Na-Sn all-solid-state cells tested at an elevated temperature of 60 °C showed increased capacities (Figure S7). Importantly, the electrodes using BM-Li_2ZrCl_6 outperformed those using Na_3PS_4 as well. Specifically, the ICE and the capacity retention at 22nd cycle for using BM-Li_2ZrCl_6 were as high as 98.4% and 96.8%, respectively. These values are even higher than those at 30 °C (93.1% and 83.7%, respectively), which is indebted to more facilitated Na^+ conduction in

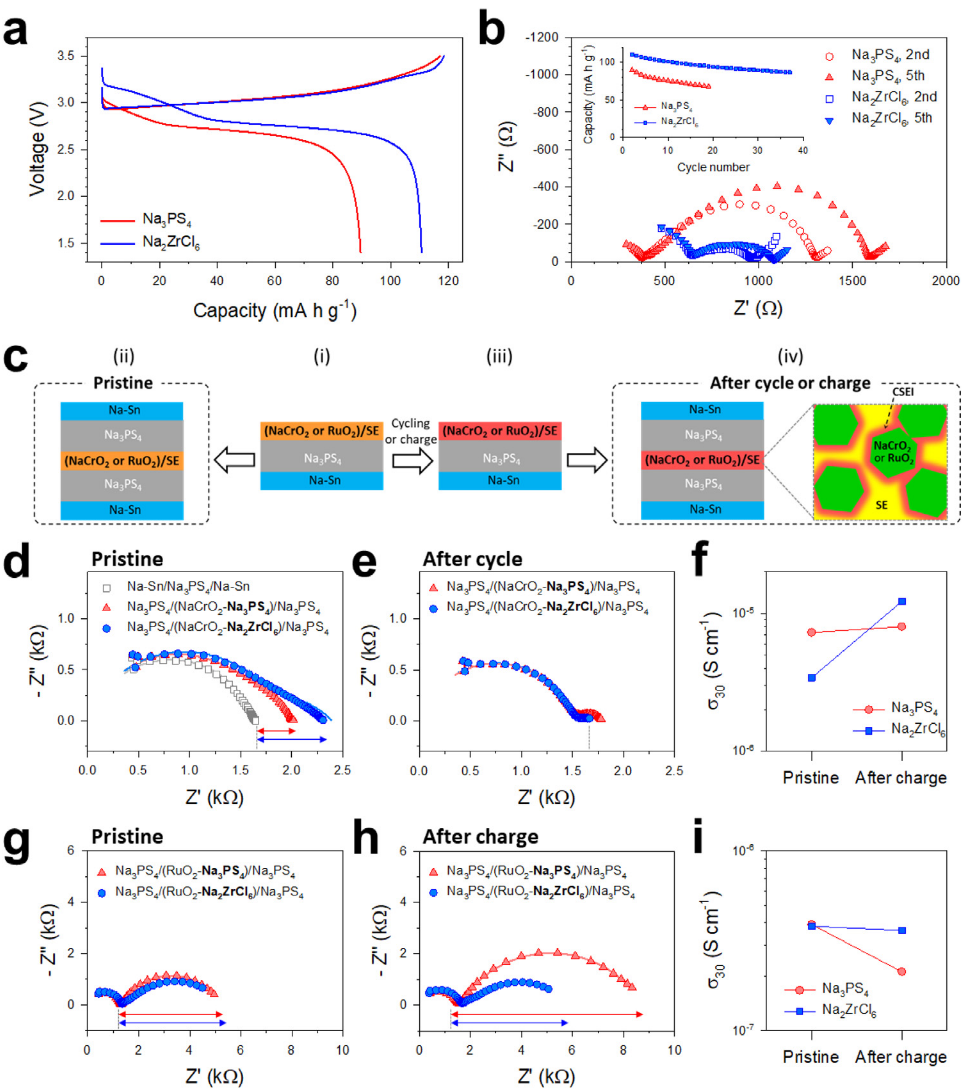

Fig. 4. Electrochemical characterization of the $NaCrO_2$/Na-Sn all-solid-state cells employing BM-Na_2ZrCl_6 and Na_3PS_4 at 30°C. a) First-cycle charge–discharge voltage profiles at 0.1 C for the $NaCrO_2$ electrodes using BM-Na_2ZrCl_6 and Na_3PS_4 and b) corresponding Nyquist plots. Cycling performance at 0.1 C is also shown in the inset. c) Schematic illustrating the EIS measurements of Na^+ non-blocking e^--blocking symmetric cells of Na-Sn/Na_3PS_4/electrode/Na_3PS_4/Na-Sn for $NaCrO_2$ or RuO_2 electrodes using Na_3PS_4 or BM-Na_2ZrCl_6. Nyquist plots of the symmetric cells for $NaCrO_2$ d) before cycling and e) after initial cycle, and f) corresponding Na^+ conductivities at 30 °C. Nyquist plots of the symmetric cells for the RuO_2 electrodes g) before cycling and h) after first charge, and i) corresponding Na^+ conductivities at 30 °C. The arrows in (d, e, g, h) indicate the contribution by the electrodes only.

the electrodes at the elevated temperature of 60 °C (6.6×10^{-5} S cm^{-1} vs. 1.8×10^{-5} S/cm at 30 °C). To assess the cathode–SE interfacial stabilities between $NaCrO_2$ and the two different SEs, BM-Na_2ZrCl_6 and Na_3PS_4, electrochemical impedance spectroscopy (EIS) measurements were conducted. As presented in Fig. 4b, the corresponding Nyquist plots in the 2nd and 5th cycles show that the size of the semicircles for the $NaCrO_2$ electrodes employing Na_3PS_4 (corresponding to the interfacial resistance at the $NaCrO_2$-SE interface) is much larger (~933 Ω) than that observed when using BM-Na_2ZrCl_6 (~320 Ω).

To further evaluate the effects of interfacial irreversible reactions on the electrochemical performance, largely varied by the types of SEs, Na_3PS_4 vs. Na_2ZrCl_6, EIS experiments were carried out using Na^+ non-blocking e^--blocking symmetric cells of Na-Sn/Na_3PS_4/electrode/Na_3PS_4/Na-Sn for $NaCrO_2$ or RuO_2 electrodes using Na_3PS_4 or BM-Na_2ZrCl_6 before cycling and after cycle or charge (Fig. 4c). Resulting Nyquist plots and corresponding Na^+ conductivities for the $NaCrO_2$ electrodes are shown in Fig. 4d-f. The equivalent circuit model and the fitted results are also provided in Figure S8 and Table S2. It was anticipated that the formation of interfacial side-reaction products, i.e., cathode SE interphase (CSEI) indicated in Fig. 4c, would lead to an overall decrease in Na^+ conductivity of the electrodes after charge. For the $NaCrO_2$ electrodes, while Na^+ conductivity for using Na_3PS_4 remained with a marginal change after initial cycle, Na^+ conductivity increased significantly for using Na_2ZrCl_6 (from 3.4×10^{-6} to 1.2×10^{-5} S cm^{-1}). This result indicates the advantageous feature of Na_2ZrCl_6 over Na_3PS_4 in terms of intactness. However, the even increasing Na^+ conductivity after initial cycle when using Na_2ZrCl_6 reflects the appreciable contribution by $Na_{1-x}CrO_2$, that is, the partially desodiated $Na_{1-x}CrO_2$ would show higher Na^+ diffusivity than pristine $NaCrO_2$ [62]. Thus, to eliminate the contribution of the cathode active material, electrodes employing Na^+-inactive but e^--conductive RuO_2 were also tested and corresponding results are presented in Fig. 4g-i. The loss of Na^+ conductivity was significant when using Na_3PS_4 (from 3.9×10^{-7} to 2.1×10^{-7} S cm^{-1}) which is in stark contrast to the marginal change when using Na_2ZrCl_6 (from 3.8×10^{-7} to 3.6×10^{-7} S cm^{-1}). These results clearly demonstrate the intactness of Na_2ZrCl_6 and the severe side reaction of Na_3PS_4 when applied for 3 V cathodes, which also agrees perfectly with the drastic differences in interfacial resistances in the Nyquist plots for half cells in Fig. 4b.

The underlying interfacial (electro)chemical evolution was probed by ex situ X-ray photoelectron spectroscopy (XPS) measurements of the $NaCrO_2$ electrodes employing Na_3PS_4 and BM-Na_2ZrCl_6 before and after 10 cycles (Fig. 5). For the electrodes using Na_3PS_4 after cycling (Fig. 5a), both S 2p and P 2p XPS spectra exhibited the evolution of the oxidized species of SO_4^{2-}, PO_4^{3-}, bridging sulfur (P-$[S]_n$-P), and P_2S_5, derived from Na_3PS_4, and this result is consistent with that reported in the previous reports on electrodes using Li^+-conducting sulfide SEs [31,63]. In contrast, for both Zr 3d and Cl 2p spectra (Fig. 5b), marginal changes were observed after 10 cycles, corroborating the intactness of Na_2ZrCl_6. Briefly, the electrochemical and ex situ XPS measurements unambigu-

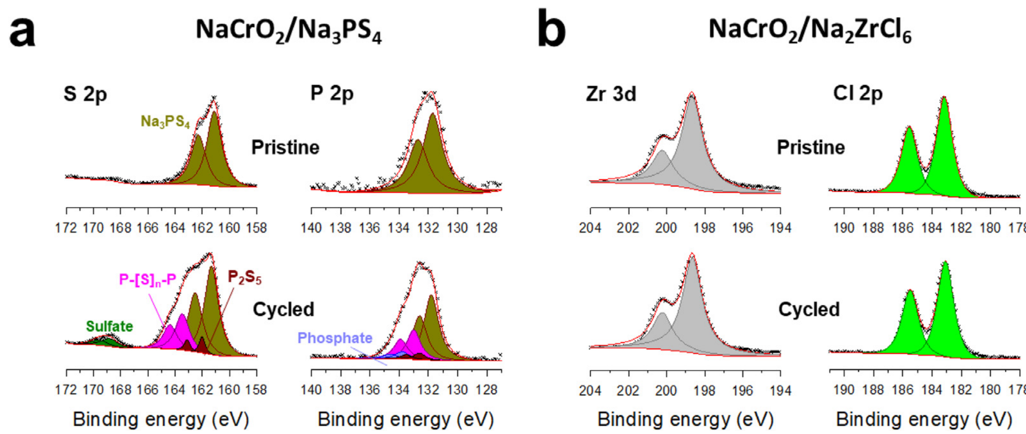

Fig. 5. Ex situ XPS signals of the $NaCrO_2$ electrodes employing a) Na_3PS_4 and b) BM-Na_2ZrCl_6 before and after 10 cycles.

ously confirm the excellent stability of Na_2ZrCl_6 when operated in contact with $NaCrO_2$ up to ~3.6 V (vs. Na/Na^+).

3. Conclusions

In summary, a new Na^+-conducting halide SE, Na_2ZrCl_6 with a maximum Na^+ conductivity of 1.8×10^{-5} S cm^{-1} was prepared by a mechanochemical method. Rietveld XRD refinements of the heat-treated Na_2ZrCl_6 identified the trigonal structure of a space group of P$\bar{3}$m1 with the fully ordered metal (Zr1 and Zr2) and Na sites. Moreover, BVEL calculation results revealed the 1D-preferable Na^+ migration pathways parallel to the c-axis via the Na^+ interstitial sites. Finally, the promising electrochemical performance of $NaCrO_2$/Na-Sn all-solid-state cells using Na_2ZrCl_6, especially in terms of high ICEs of 93.1 and 98.4% at 30 and 60 °C, respectively, was highlighted. The intactness of Na_2ZrCl_6 with $NaCrO_2$ up to ~3.6 V (vs. Na/Na^+) was also confirmed by ex situ XPS measurements. Despite the comparably low Na^+ conductivity of Na_2ZrCl_6, a highly desirable electrochemical performance was demonstrated, which emphasizes the importance of cathode–SE interfacial stability in all-solid-state batteries. Further improvements in Na^+ conductivity, such as aliovalent and/or isovalent substitutions, are required for this new halide SE, Na_2ZrCl_6, similar to that required for halide Li counterparts [40,43,53] and Na^+-conducting sulfide SEs.[8,9,17,18,23,25].

4. Experimental

4.1. Preparation of materials

For the preparation of Na_2ZrCl_6, a stoichiometric mixture of NaCl (99.99%, Alfa Aeser) and $ZrCl_4$ (99.99%, Sigma Aldrich) was ball-milled at 600 rpm for 10 h in a ZrO_2 vial with ZrO_2 balls using Pulverisette 7PL (Fritsch GmbH). For further heat treatment, the ball-milled powders were annealed at 400°C for 12 h in a fused silica ampule sealed under vacuum. Na_3PS_4 powders were prepared by ball milling a stoichiometric mixture of Na_2S (Sigma Aldrich) and P_2S_5 (99%, Sigma Aldrich), followed by heat treatment at 270 °C for 1 h in a fused silica ampule sealed under vacuum. For the preparation of $Na_4(B_{12}H_{12})(B_{10}H_{10})$, a stoichiometric mixture of pre-dried $Na_2B_{12}H_{12}$ and $Na_2B_{10}H_{10}$ (Katchem) was first dissolved in anhydrous isopropanol (99.9%, VWR), subsequently dried in a rotary evaporator, and heat-treated at 180°C for 4 h under vacuum [59,64]. RuO_2 powders with a particle size of < ~100 nm (99.9%, Sigma Aldrich) were used for Na^+-non-blocking e^--blocking symmetric cells.

4.2. Materials characterization

The powder XRD patterns were collected using a Rigaku MiniFlex 600 diffractometer with Cu Kα radiation (λ = 1.54059 Å). XRD cells containing hermetically sealed SE samples with a beryllium window were mounted on an XRD diffractometer and measured at 40 kV and 15 mA. Powder XRD data for Rietveld refinement were collected at room temperature on a Bragg–Brentano X-ray diffractometer (PANalytical Empyrean) with Cu Kα_1 X-ray radiation, a focusing primary Ge (111) monochromator (λ = 1.54059 Å), and a position-sensitive PIXcel 3D 2 × 2 detector. Data acquisition covered the angular range 10° ≤ 2θ ≤ 130° at a step width of 0.0131303° and a total measurement time of 13 h. Powder sampling for X-ray measurement was conducted in an Ar atmosphere glovebox, and an airtight specimen dome-type X-ray sample holder obtained from Bruker was used to protect our sample from air during the measurement. The crystal structure of Na_2ZrCl_6 was determined from the powder XRD data, using a combination of the powder profile refinement program GSAS [65,66] and the single-crystal structure refinement program CRYSTALS,[67] as described in our previous work [68,69]. For a three-dimensional (3D) view of the Fourier density maps, MCE was used [70]. A trigonal unit cell was determined using the program Dicvol [71] run in WinPLOTR [63] using 12 diffraction peaks. Le Bail fitting was performed for the new phase. Initially, a structure model with only a dummy atom at an arbitrary position in the unit cell was used. Subsequently, Le Bail fitting was performed to obtain the structure factor of each (hkl) reflection. The obtained structure factors were employed as the input data for CRYSTALS. In this case, a direct method was used for the initial phasing model using SHELX [72] run in CRYSTALS, which yielded several metal positions and not all atoms at once. The partial structural model replaced the initial dummy-atom model, and it was used for a Le Bail fit in GSAS again (step 1). Subsequently, improved structure factors were obtained, and refinement was performed in CRYSTALS (step 2). Steps 1 and 2 were repeated until a complete and satisfactory structure model was obtained. Finally, Rietveld refinement in GSAS was performed to complete structure determination, resulting in reasonable isotropic displacement parameters and agreement indices for Na_2ZrCl_6. The bond valence sums [73,74] for each atom in Na_2ZrCl_6 were calculated with the program SoftBV [75] to validate the structure of Na_2ZrCl_6. The BVEL calculation was also performed using SoftBV. The BVEL results show the energy barrier for Na ions and the plausible diffusion pathways by 3D graphics.

4.3. Electrochemical characterization

The Na^+ conductivity was measured by the AC impedance method using ion-blocking Ti/SE/Ti symmetric cells under ~70 MPa. The cold-pressed pellets were prepared at 370 MPa. The EIS data were recorded with an amplitude of 100 mV and a frequency range from 10 mHz to 7 MHz using a VMP3 (Bio-Logic). All-solid-state $NaCrO_2$/Na-Sn half-cells were fabricated using the following procedure: Na–Sn (nominal composition: Na_3Sn) was used as the counter and reference electrodes, which was prepared by mixing Na metal (Sigma Aldrich) with Sn metal powders (Sigma Aldrich). Composite electrodes were prepared from a $NaCrO_2$/BM-Na_2ZrCl_6 or Na_3PS_4 mixture in a weight ratio of 94:56. The separating SE layers were formed by pelletizing 100 mg of Na_3PS_4 powders under 370 MPa. To prevent degradation between Na_3PS_4 and Na-Sn, Na_3PS_4 (100 mg)/$Na_4(B_{12}H_{12})(B_{10}H_{10})$ (25 mg) was used.[59] Subsequently, the $NaCrO_2$ electrodes and the Na–Sn electrodes were placed on each side of the SE layers to form ($NaCrO_2$/BM-Na_2ZrCl_6 or Na_3PS_4)/(Na_3PS_4/$Na_4(B_{12}H_{12})(B_{10}H_{10})$)/Na-Sn assemblies. Finally, the whole assemblies were pressed at 370 MPa, forming all-solid-state $NaCrO_2$/Na–Sn cells. The galvanostatic discharge–charge cycling of the all-solid-state $NaCrO_2$/Na–Sn cells was conducted in the voltage range of 1.4–3.5 V under ~70 MPa. All the procedures to fabricate all-solid-state cells were performed in a polyaryletheretherketone (PEEK) mold (diameter = 13 mm) with Ti rods as the current collectors. All electrochemical tests were conducted at 30°C. The EIS measurements for the half cells were performed from 1.5 MHz to 5 mHz with 10 mV of amplitude after discharging the cells to 2.85 V for Na_2ZrCl_6 and to 2.80 V for Na_3PS_4/$Na_4(B_{12}H_{12})(B_{10}H_{10})$ at 0.1C at the second and fifth cycle. Na^+ non-blocking e^--blocking symmetric cells of Na-Sn/Na_3PS_4/electrode/Na_3PS_4/Na-Sn for $NaCrO_2$ or RuO_2 electrodes using Na_3PS_4 or BM-Na_2ZrCl_6 were fabricated as follows. The separating SE layers were formed by pelletizing 150 mg of Na_3PS_4 powders under 370 MPa. Na–Sn (nominal composition: Na_3Sn) was used as the counter and reference electrodes. Composite electrodes were prepared by manual mixing of $NaCrO_2$ and BM-Na_2ZrCl_6 or Na_3PS_4 in a weight ratio of 94:56 or RuO_2 and BM-Na_2ZrCl_6 or Na_3PS_4 in a vol. ratio of 7:3. Subsequently, the composite electrodes and the Na–Sn electrodes were placed on each side of the SE layers to form electrode/Na_3PS_4/Na-Sn assemblies, which was followed by pressing the whole assemblies pressing at 370 MPa (Fig. 4c (i)). For the EIS measurements of the pristine electrodes (Fig. 4c (ii)), after 150 mg of Na_3PS_4 powders were put on the electrode side, the assemblies were pelletized. Then, Na-Sn was placed on the Na_3PS_4 layer, followed by pressing at 370 MPa. The as-assembled Na-Sn/Na_3PS_4/electrode/Na_3PS_4/Na-Sn symmetric cells were subjected to the EIS measurements. For the EIS measurements of the cycled or charged electrodes (Fig. 4c (iv)), before stacking Na_3PS_4 and Na-Sn layers on the electrodes, electrode/Na_3PS_4/Na-Sn cells were charged to 3.6 V at 0.1C and 30°C . The EIS data for the symmetric cells were recorded under ~70 MPa with an amplitude of 10 mV and a frequency range from 100 mHz to 7 MHz using a VMP3 (Bio-Logic).

Declaration of Competing Interest

The authors declare that they have no known competing financial interests or personal relationships that could have appeared to influence the work reported in this paper.

CRediT authorship contribution statement

Hiram Kwak: Conceptualization, Methodology, Methodology, Investigation, Writing - original draft. **Jeyne Lyoo:** Methodology, Investigation, Writing - original draft. **Juhyoun Park:** Investigation. **Yoonjae Han:** Data curation. **Ryo Asakura:** Resources. **Arndt Remhof:** Resources, Writing - review & editing. **Corsin Battaglia:** Resources, Writing - review & editing. **Hansu Kim:** Writing - review & editing. **Seung-Tae Hong:** Supervision, Writing - review & editing. **Yoon Seok Jung:** Conceptualization, Supervision, Writing - review & editing.

Acknowledgements

This research was supported by the Technology Development Program to Solve Climate Changes and by Basic Science Research Program of the National Research Foundation (NRF) funded by the Ministry of Science & ICT (grant no. NRF-2017M1A2A2044501 and 2018R1A2B6004996), and by the Materials and Components Technology Development Program of MOTIE/KEIT (grant no. 20007045 and 20012216).

Supplementary materials

Supplementary material associated with this article can be found, in the online version, at doi:10.1016/j.ensm.2021.01.026.

References

[1] A. Hayashi, K. Noi, A. Sakuda, M. Tatsumisago, Superionic glass-ceramic electrolytes for room-temperature rechargeable sodium batteries, Nat. Commun. 3 (2012) 856, doi:10.1038/ncomms1843.
[2] Y.S. Jung, D.Y. Oh, Y.J. Nam, K.H. Park, Issues and Challenges for Bulk-Type All-Solid-State Rechargeable Lithium Batteries using Sulfide Solid Electrolytes, Israel J. Chem. 55 (2015) 472–485, doi:10.1002/ijch.201400112.
[3] A. Banerjee, K.H. Park, J.W. Heo, Y.J. Nam, C.K. Moon, S.M. Oh, S.T. Hong, Y.S. Jung, Na_3SbS_4: A Solution Processable Sodium Superionic Conductor for All-Solid-State Sodium-Ion Batteries, Angew. Chem. Int. Ed. 128 (2016) 9786–9790, doi:10.1002/ange.201604158.
[4] L. Duchêne, R.-S. Kühnel, E. Stilp, E.C. Reyes, A. Remhof, H. Hagemann, C. Battaglia, A stable 3 V all-solid-state sodium–ion battery based on a closo-borate electrolyte, Energy Environ. Sci. 10 (2017) 2609–2615, doi:10.1039/C7EE02420G.
[5] K.H. Park, Q. Bai, D.H. Kim, D.Y. Oh, Y. Zhu, Y. Mo, Y.S. Jung, Design strategies, practical considerations, and new solution processes of sulfide solid electrolytes for all-solid-state batteries, Adv. Energy Mater. 8 (2018) 1800035, doi:10.1002/aenm.201800035.
[6] X. Chi, Y. Liang, F. Hao, Y. Zhang, J. Whiteley, H. Dong, P. Hu, S. Lee, Y. Yao, Tailored Organic Electrode Material Compatible with Sulfide Electrolyte for Stable All-Solid-State Sodium Batteries, Angew. Chem. Int. Ed. 57 (2018) 2630–2634, doi:10.1002/anie.201712895.
[7] J.J. Kim, K. Yoon, I. Park, K. Kang, Progress in the Development of Sodium-Ion Solid Electrolytes, Small Methods 1 (2017) 1700219, doi:10.1002/smtd.201700219.
[8] J.W. Heo, A. Banerjee, K.H. Park, Y.S. Jung, S.T. Hong, New Na-Ion Solid Electrolytes $Na_{4-x}Sn_{1-x}Sb_xS_4$ ($0.02 \leq x \leq 0.33$) for All-Solid-State Na-Ion Batteries, Adv. Energy Mater. 8 (2018) 1702716, doi:10.1002/aenm.20170271.
[9] A. Hayashi, N. Masuzawa, S. Yubuchi, F. Tsuji, C. Hotehama, A. Sakuda, M. Tatsumisago, A sodium-ion sulfide solid electrolyte with unprecedented conductivity at room temperature, Nat. Commun. 10 (2019) 1–6, doi:10.1038/s41467-019-13178-2.
[10] K. Xu, Nonaqueous liquid electrolytes for lithium-based rechargeable batteries, Chem. Rev. 104 (2004) 4303–4417, doi:10.1021/cr030203g.
[11] Y. Kato, S. Hori, T. Saito, K. Suzuki, M. Hirayama, A. Mitsui, M. Yonemura, H. Iba, R. Kanno, High-power all-solid-state batteries using sulfide superionic conductors, Nat. Energy 1 (2016) 1–7, doi:10.1038/nenergy.2016.30.
[12] L. Duchene, A. Remhof, H. Hagemann, C. Battaglia, Status and prospects of hydroborate electrolytes for all-solid-state batteries, Energy Storage Mater 25 (2020) 782–794, doi:10.1016/j.ensm.2019.08.032.
[13] J.B. Goodenough, H.Y.P. Hong, J.A. Kafalas, Fast Na^+-ion transport in skeleton structures, Mater. Res. Bull. 11 (1976) 203–220, doi:10.1016/0025-5408(76)90077-5.
[14] S.K. Pal, R. Saha, G.V. Kumar, S. Omar, Designing High Ionic Conducting NASICON-type $Na_3Zr_2Si_2PO_{12}$ Solid-Electrolytes for Na-Ion Batteries, J. Phys. Chem. C 124 (2020) 9161–9169, doi:10.1021/acs.jpcc.0c00543.
[15] C. Huang, G. Yang, W. Yu, C. Xue, Y. Zhai, W. Tang, N. Hu, Z. Wen, L. Lu, S. Song, Gallium-substituted Nasicon $Na_3Zr_2Si_2PO_{12}$ solid electrolytes, J. Alloys Compd. 855 (2021) 157501, doi:10.1016/j.jallcom.2020.157501.
[16] T.W. Kim, K.H. Park, Y.E. Choi, J.Y. Lee, Y.S. Jung, Aqueous-solution synthesis of Na_3SbS_4 solid electrolytes for all-solid-state Na-ion batteries, J. Mater. Chem. A 6 (2018) 840–844, doi:10.1039/C7TA09242C.
[17] C.K. Moon, H.-J. Lee, K.H. Park, H. Kwak, J.W. Heo, K. Choi, H. Yang, M.-S. Kim, S.-T. Hong, J.H. Lee, Y.S. Jung, Vacancy-Driven Na^+ Superionic Conduction in New Ca-Doped Na_3PS_4 for All-Solid-State Na-Ion Batteries, ACS Energy Lett 3 (2018) 2504–2512, doi:10.1021/acsenergylett.8b01479.
[18] I.-H. Chu, C.S. Kompella, H. Nguyen, Z. Zhu, S. Hy, Z. Deng, Y.S. Meng, S.P. Ong, Room-temperature all-solid-state rechargeable sodium-ion batteries with a Cl-doped Na_3PS_4 superionic conductor, Sci. Rep. 6 (2016) 33733, doi:10.1038/srep33733.
[19] H.J. Deiseroth, S.T. Kong, H. Eckert, J. Vannahme, C. Reiner, T. Zaiss, M. Schlosser, Li_6PS_5X: a class of crystalline Li-rich solids with an unusually high Li^+ mobility, Angew. Chem. Int. Ed. 47 (2008) 755–758, doi:10.1002/anie.200703900.
[20] K.H. Park, D.Y. Oh, Y.E. Choi, Y.J. Nam, L. Han, J.Y. Kim, H. Xin, F. Lin, S.M. Oh, Y.S. Jung, Solution-Processable Glass LiI-Li_4SnS_4 Superionic Conductors for All-Solid-State Li-Ion Batteries, Adv. Mater. 28 (2016) 1874–1883, doi:10.1002/adma.201505008.
[21] H.-D. Lim, X. Yue, X. Xing, V. Petrova, M. Gonzalez, H. Liu, P. Liu, Designing solution chemistries for the low-temperature synthesis of sulfide-based solid electrolytes, J. Mater. Chem. A 6 (2018) 7370–7374, doi:10.1039/c8ta01800f.
[22] S. Jun, Y.J. Nam, H. Kwak, K.T. Kim, D.Y. Oh, Y.S. Jung, Operando Differential Electrochemical Pressiometry for Probing Electrochemo-mechanics in All-Solid-State Batteries, Adv. Funct. Mater. (2020), doi:10.1002/adfm.202002535.

[23] N. Tanibata, K. Noi, A. Hayashi, M. Tatsumisago, Preparation and characterization of highly sodium ion conducting Na_3PS_4–Na_4SiS_4 solid electrolytes, Rsc Adv 4 (2014) 17120–17123, doi:10.1039/C4RA00996G.
[24] L. Zhang, K. Yang, J. Mi, L. Lu, L. Zhao, L. Wang, Y. Li, H. Zeng, Na_3PSe_4: A novel chalcogenide solid electrolyte with high ionic conductivity, Adv. Energy Mater. 5 (2015) 1501294, doi:10.1002/aenm.201501294.
[25] Z. Yu, S.L. Shang, J.H. Seo, D. Wang, X. Luo, Q. Huang, S. Chen, J. Lu, X. Li, Z.K. Liu, D. Wang, Exceptionally High Ionic Conductivity in $Na_3P_{0.62}As_{0.38}S_4$ with Improved Moisture Stability for Solid-State Sodium-Ion Batteries, Adv. Mater 29 (2017) 1605561, doi:10.1002/adma.201605561.
[26] Z. Zhu, I.-H. Chu, Z. Deng, S.P. Ong, Role of Na^+ interstitials and dopants in enhancing the Na^+ conductivity of the cubic Na_3PS_4 superionic conductor, Chem. Mater. 27 (2015) 8318–8325, doi:10.1021/acs.chemmater.5b03656.
[27] C. Yu, S. Ganapathy, N.J.J. de Klerk, E.R.H. van Eck, M. Wagemaker, Na-ion dynamics in tetragonal and cubic Na_3PS_4, a Na-ion conductor for solid state Na-ion batteries, J. Mater. Chem. A 4 (2016) 15095–15105, doi:10.1039/c6ta05896e.
[28] M. Duchardt, U. Ruschewitz, S. Adams, S. Dehnen, B. Roling, Vacancy-Controlled Na^+ Superion Conduction in $Na_{11}Sn_2PS_{12}$, Angew. Chem. Int. Ed. 57 (2018) 1351–1355, doi:10.1002/anie.201712769.
[29] Z. Zhang, E. Ramos, F. Lalère, J. Assoud, K. Kaup, P. Hartman, L.F. Nazar, $Na_{11}Sn_2PS_{12}$:a new solid state sodium superionic conductor, Energy Environ. Sci. 11 (2018) 87–93, doi:10.1039/C7EE03083E.
[30] Y. Zhu, X. He, Y. Mo, Origin of Outstanding Stability in the Lithium Solid Electrolyte Materials: Insights from Thermodynamic Analyses Based on First-Principles Calculations, ACS Appl. Mater. Interfaces 7 (2015) 23685–23693, doi:10.1021/acsami.5b07517.
[31] S.H. Jung, K. Oh, Y.J. Nam, D.Y. Oh, P. Brüner, K. Kang, Y.S. Jung, Li_3BO_3–Li_2CO_3: rationally designed buffering phase for sulfide all-solid-state Li-ion batteries, Chem. Mater. 30 (2018) 8190–8200, doi:10.1021/acs.chemmater.8b03321.
[32] Y. Xiao, Y. Wang, S.-H. Bo, J.C. Kim, L.J. Miara, G. Ceder, Understanding interface stability in solid-state batteries, Nat. Rev. Mater. 5 (2020) 105–126, doi:10.1038/s41578-019-0157-5.
[33] A. Sakuda, A. Hayashi, M.J.C. o. M. Tatsumisago, Interfacial observation between $LiCoO_2$ electrode and Li_2S– P_2S_5 solid electrolytes of all-solid-state lithium secondary batteries using transmission electron microscopy, Chem. Mater. 22 (2010) 949–956, doi:10.1021/cm901819c.
[34] F. Walther, R. Koerver, T. Fuchs, S. Ohno, J. Sann, M. Rohnke, W.G. Zeier, J. Janek, Visualization of the interfacial decomposition of composite cathodes in argyrodite based all-solid-state batteries using time-of-flight secondary ion mass spectrometry, Chem. Mater. 31 (2019) 3745–3755, doi:10.1021/acs.chemmater.9b00770.
[35] Y. Tian, T. Shi, W.D. Richards, J. Li, J.C. Kim, S.-H. Bo, G. Ceder, Compatibility issues between electrodes and electrolytes in solid-state batteries, Energy Environ. Sci. 10 (2017) 1150–1166, doi:10.1039/C7EE00534B.
[36] X. Li, J. Liang, X. Yang, K.R. Adair, C. Wang, F. Zhao, X. Sun, Progress and Perspectives for Halide Solid-State Electrolyte for All-Solid-State Lithium Batteries, Energy Environ. Sci. 13 (2020) 1429–4161, doi:10.1039/C9EE03828K.
[37] S. Wang, Q. Bai, A.M. Nolan, Y. Liu, S. Gong, Q. Sun, Y. Mo, Lithium Chlorides and Bromides as Promising Solid-State Chemistries for Fast Ion Conductors with Good Electrochemical Stability, Angew. Chem. Int. Ed. 58 (2019) 8039–8043, doi:10.1002/anie.201901938.
[38] T. Asano, A. Sakai, S. Ouchi, M. Sakaida, A. Miyazaki, S. Hasegawa, Solid Halide Electrolytes with High Lithium-Ion Conductivity for Application in 4 V Class Bulk-Type All-Solid-State Batteries, Adv. Mater. 30 (2018) e1803075, doi:10.1002/adma.201803075.
[39] X. Li, J. Liang, J. Luo, M. Norouzi Banis, C. Wang, W. Li, S. Deng, C. Yu, F. Zhao, Y. Hu, T.-K. Sham, L. Zhang, S. Zhao, S. Lu, H. Huang, R. Li, K.R. Adair, X. Sun, Air-stable Li_3InCl_6 electrolyte with high voltage compatibility for all-solid-state batteries, Energy Environ. Sci. 12 (2019) 2665–2671, doi:10.1039/c9ee02311a.
[40] K.H. Park, K. Kaup, A. Assoud, Q. Zhang, X. Wu, L.F. Nazar, High-Voltage Superionic Halide Solid Electrolytes for All-Solid-State Li-Ion Batteries, ACS Energy Lett 5 (2020) 533–539, doi:10.1021/acsenergylett.9b02599.
[41] J. Liang, X. Li, S. Wang, K.R. Adair, W. Li, Y. Zhao, C. Wang, Y. Hu, L. Zhang, S. Zhao, S. Lu, H. Huang, R. Li, Y. Mo, X. Sun, Site-Occupation-Tuned Superionic Li_xScCl_{3+x}Halide Solid Electrolytes for All-Solid-State Batteries, J. Am. Chem. Soc. 142 (2020) 7012–7022, doi:10.1021/jacs.0c00134.
[42] L. Zhou, C.Y. Kwok, A. Shyamsunder, Q. Zhang, X. Wu, L.F. Nazar, A new halospinel superionic conductor for high-voltage all solid state lithium batteries, Energy Environ. Sci. 13 (2020) 2056–2063, doi:10.1039/d0ee01017k.
[43] H. Kwak, D. Han, J. Lyoo, J. Park, S.H. Jung, Y. Han, G. Kwon, H. Kim, S.-T. Hong, K.-W. Nam, Y.S. Jung, New cost-effective halide solid electrolytes for all-solid-state batteries: mechanochemically prepared Fe^{3+}-substituted Li_2ZrCl_6, Adv. Energy Mater. (2021) 2003190 in press, doi:10.1002/aenm.202003190.
[44] R. Schlem, S. Muy, N. Prinz, A. Banik, Y. Shao-Horn, M. Zobel, W.G. Zeier, Mechanochemical Synthesis: A Tool to Tune Cation Site Disorder and Ionic Transport Properties of Li_3MCl_6 (M = Y, Er) Superionic Conductors, Adv. Energy Mater. 10 (2019) 1903719, doi:10.1002/aenm.201903719.
[45] A. Bohnsack, F. Stenzel, A. Zajonc, G. Balzer, M.S. Wickleder, G. Meyer, Ternre Halogenide vom Typ A_3MX_6. VI [1].Ternre Chloride der Selten-Erd-Elemente mit Lithium, Li_3MCl_6 (M = Tb-Lu, Y, Sc): Synthese, Kristallstrukturen und Ionenbewegung, Z. Anorg, Allg. Chem 623 (1997) 1067–1073, doi:10.1002/zaac.19976230710.
[46] R.D. Shannon, Revised effective ionic radii and systematic studies of interatomic distances in halides and chalcogenides, Acta Cryst. A 32 (1976) 751–767, doi:10.1107/S0567739476001551.
[47] G.M. Photiadis, G.N. Papatheodorou, Vibrational modes and structure of liquid and gaseous zirconium tetrachloride and of molten $ZrCl_4$–CsCl mixtures, Dalton Trans (1998) 981–990, doi:10.1039/a707126d.
[48] G. Papatheodorou, Raman spectroscopic studies of yttrium (III) chloride–alkali metal chloride melts and of Cs_2NaYCl_6 and YCl_3 solid compounds, J. Chem. Phys. 66 (1977) 2893–2900, doi:10.1063/1.434359.
[49] K. Biswas, M.-H. Du, Energy transport and scintillation of cerium-doped elpasolite Cs_2LiYCl_6: Hybrid density functional calculations, Physical Review B 86 (2012) 014102, doi:10.1103/PhysRevB.86.014102.
[50] I.D. Brown, Recent Developments in the Methods and Applications of the Bond Valence Model, Chem. Rev. 109 (2009) 6858–6919, doi:10.1021/cr900053k.
[51] H. Kwak, K.H. Park, D. Han, K.-W. Nam, H. Kim, Y.S. Jung, Li^+ conduction in air-stable Sb-Substituted Li_4SnS_4 for all-solid-state Li-Ion batteries, J. Power Sources 446 (2020) 227338, doi:10.1016/j.jpowsour.2019.227338.
[52] M. Avdeev, M. Sale, S. Adams, R.P. Rao, Screening of the alkali-metal ion containing materials from the Inorganic Crystal Structure Database (ICSD) for high ionic conductivity pathways using the bond valence method, Solid State Ion. 225 (2012) 43–46, doi:10.1016/j.ssi.2012.02.014.
[53] Y. Liu, S. Wang, A.M. Nolan, C. Ling, Y. Mo, Tailoring the Cation Lattice for Chloride Lithium-Ion Conductors, Adv. Energy Mater. 10 (2020) 2002356, doi:10.1002/aenm.202002356.
[54] X. He, Y. Zhu, Y. Mo, Origin of fast ion diffusion in super-ionic conductors, Nat. Commun. 8 (2017) 15893, doi:10.1038/ncomms15893.
[55] T. Famprikis, P. Canepa, J.A. Dawson, M.S. Islam, C. Masquelier, Fundamentals of inorganic solid-state electrolytes for batteries, Nat. Mater. 18 (2019) 1278–1291, doi:10.1038/s41563-019-0431-3.
[56] W.D. Richards, Y. Wang, L.J. Miara, J.C. Kim, G. Ceder, Design of $Li_{1+2x}Zn_{1-x}PS_4$, a new lithium ion conductor, Energy Environ. Sci. 9 (2016) 3272–3278, doi:10.1039/C6EE02094A.
[57] Y. Wang, W.D. Richards, S.P. Ong, L.J. Miara, J.C. Kim, Y. Mo, G. Ceder, Design principles for solid-state lithium superionic conductors, Nat. Mater. 14 (2015) 1026–1031, doi:10.1038/nmat4369.
[58] S. Anwane, Solid Electrolytes: Principles and Applications, 2014. 259-294
[59] L. Duchene, D.H. Kim, Y.B. Song, S. Jun, R. Moury, A. Remhof, H. Hagemann, Y.S. Jung, C. Battaglia, Crystallization of closo-borate electrolytes from solution enabling infiltration into slurry-casted porous electrodes for all-solid-state batteries, Energy Storage Mater 26 (2020) 543–549, doi:10.1016/j.ensm.2019.11.027.
[60] V.L. Chevrier, G. Ceder, Challenges for Na-ion Negative Electrodes, J. Electrochem. Soc. 158 (2011) A1011, doi:10.1149/1.3607983.
[61] C.-Y. Yu, J.-S. Park, H.-G. Jung, K.-Y. Chung, D. Aurbach, Y.-K. Sun, S.-T. Myung, $NaCrO_2$ cathode for high-rate sodium-ion batteries, Energy Environ. Sci. 8 (2015) 2019–2026, doi:10.1039/c5ee00695c.
[62] H. Xia, L. Lu, G. Ceder, Li diffusion in $LiCoO_2$ thin films prepared by pulsed laser deposition, J. Power Sources 159 (2006) 1422–1427, doi:10.1016/j.jpowsour.2005.12.012.
[63] S.H. Jung, U.-H. Kim, J.-H. Kim, S. Jun, C.S. Yoon, Y.S. Jung, Y.-K. Sun, Ni-Rich Layered Cathode Materials with Electrochemo-Mechanically Compliant Microstructures for All-Solid-State Li Batteries, Adv. Energy Mater. 10 (2020) 1903360, doi:10.1002/aenm.201903360.
[64] R. Asakura, L. Duchene, R.S. Kuhnel, A. Remhof, H. Hagemann, C. Battaglia, Electrochemical Oxidative Stability of Hydroborate-Based Solid State Electrolytes, ACS Appl. Energy Mater. 2 (2019) 6924–6930, doi:10.1021/acsaem.9b01487.
[65] T. Roisnel, J. Rodríquez-Carvajal, in: Materials Science Forum, 378, Transtec Publications, 1999, pp. 118–123. **2001**.
[66] A.C. Larson, R.B. Von Dreele, Gsas, General Structure Analysis System. LANSCE, MS-H805, Los Alamos, New Mexico, 1994.
[67] P.W. Betteridge, J.R. Carruthers, R.I. Cooper, K. Prout, D.J. Watkin, CRYSTALS version 12: software for guided crystal structure analysis, J. Appl. Crystallogr. 36 (2003) 1487-1487, doi:10.1107/S0021889803021800.
[68] E. Lee, S.-T. Hong, Sr_4AlNbO_8: A new crystal structure type determined from powder X-ray data, J. Solid State Chem. 181 (2008) 2930–2934, doi:10.1016/j.jssc.2008.07.009.
[69] S.C. Lim, J. Lee, H.H. Kwak, J.W. Heo, M.S. Chae, D. Ahn, Y.H. Jang, H. Lee, S.T. Hong, Unraveling the Magnesium-Ion Intercalation Mechanism in Vanadium Pentoxide in a Wet Organic Electrolyte by Structural Determination, Inorg. Chem. 56 (2017) 7668–7678, doi:10.1021/acs.inorgchem.7b00204.
[70] M. Hušák, B. Kratochvil, MCE–program for fast interactive visualization of electron, similar density maps, optimized for small molecules, J. Appl. Crystallogr. 36 (2003) 1104-1104, doi:10.1107/S0021889803012603.
[71] A. Boultif, D. Louër, Indexing of powder diffraction patterns for low-symmetry lattices by the successive dichotomy method, J. Appl. Crystallogr. 24 (1991) 987–993, doi:10.1107/S0021889891006441.
[72] G.M. Sheldrick, A short history of SHELX, Acta Crystallogr. A 64 (2008) 112–122, doi:10.1107/S0108767307043930.
[73] I. Brown, D. Altermatt, Bond-valence parameters obtained from a systematic analysis of the inorganic crystal structure database, Acta Crystallogr. B Struct. Sci. 41 (1985) 244–247, doi:10.1107/S0108768185002063.
[74] N. Brese, M. O'keeffe, Bond-valence parameters for solids, Acta Crystallogr. B Struct. Sci. 47 (1991) 192–197, doi:10.1107/S0108768190011041.
[75] H. Chen, L.L. Wong, S. Adams, SoftBV–a software tool for screening the materials genome of inorganic fast ion conductors, Acta Crystallogr. B Struct. Sci. 75 (2019) 18–33, doi:10.1107/S2052520618015718.